Naval Research Laboratory
Washington, DC 20375-5320

NRL/6810/MR—2022/4

Computational Methods for Determining Structure and Dynamics in DNA-Scaffolded Molecular Networks

BRIAN S. ROLCZYNSKI

Quantum and Optoelectronics Branch
Electronics Science and Technology Division

December 16, 2022

REPORT DOCUMENTATION PAGE

Form Approved
OMB No. 0704-0188

1. REPORT DATE *(DD-MM-YYYY)* 16-12-2022	**2. REPORT TYPE** NRL Memorandum Report	**3. DATES COVERED** *(From - To)* 10-25-2021 – 10-24-2022

4. TITLE AND SUBTITLE

Computational Methods for Determining Structure and Dynamics in DNA-Scaffolded Molecular Networks

5a. CONTRACT NUMBER

5b. GRANT NUMBER

5c. PROGRAM ELEMENT NUMBER
NISE

6. AUTHOR(S)

Brian S. Rolczynski

5d. PROJECT NUMBER

5e. TASK NUMBER

5f. WORK UNIT NUMBER
N20Q

7. PERFORMING ORGANIZATION NAME(S) AND ADDRESS(ES)

Naval Research Laboratory
4555 Overlook Avenue, SW
Washington, DC 20375-5320

8. PERFORMING ORGANIZATION REPORT NUMBER

NRL/6810/MR--2022/4

9. SPONSORING / MONITORING AGENCY NAME(S) AND ADDRESS(ES)

Naval Research Laboratory
4555 Overlook Avenue, SW
Washington, DC 20375-5320

10. SPONSOR / MONITOR'S ACRONYM(S)

NRL/NISE

11. SPONSOR / MONITOR'S REPORT NUMBER(S)

12. DISTRIBUTION / AVAILABILITY STATEMENT

DISTRIBUTION STATEMENT A: Approved for public release; distribution is unlimited.

13. SUPPLEMENTARY NOTES

Karles Fellowship

14. ABSTRACT

This memorandum describes the research conducted by Dr. Brian Rolczynski (Code 6816) during his Jerome and Isabella Karle Distinguished Scholar Fellowship. This research developed computational methods to understand the nanoscale structural characteristics, energy levels, couplings, and related parameters for DNA-scaffolded molecular networks. Three methods are described: (1) a genetic algorithm approach to deduce the structures and Hamiltonians of molecular networks; (2) an approach based on the hierarchical equations of motion to calculate the vibronic dynamics and corresponding heat currents, which impact quantum-mechanical dephasing in these systems; (3) a Random Forest machine-learning algorithm to analyze the roles of particular molecular arrangements on the functional energy-transport processes. These methods collectively reveal the structure-dynamics-function relationships in DNA-scaffolded molecular networks, which is an important step toward optimizing these materials for uses such as quantum-mechanical technology or light-harvesting materials.

15. SUBJECT TERMS

DNA nanotechnology, machine-learning, Random Forest, genetic algorithms, hierarchical equations of motion, excitons, vibrons, chromophores, cyanines, spectroscopy, heat transfer, quantum chemistry, computational chemistry

16. SECURITY CLASSIFICATION OF:			**17. LIMITATION OF ABSTRACT**	**18. NUMBER OF PAGES**	**19a. NAME OF RESPONSIBLE PERSON** Brian Rolczynski
a. REPORT U	**b. ABSTRACT** U	**c. THIS PAGE** U	U	26	**19b. TELEPHONE NUMBER** *(include area code)* (312) 515-0821

Standard Form 298 (Rev. 8-98)
Prescribed by ANSI Std. Z39.18

This page intentionally left blank.

Table of Contents

This page intentionally left blank.

Executive Summary

This memorandum describes the research conducted by Dr. Brian Rolczynski (Code 6816) during his Jerome and Isabella Karle Distinguished Scholar Fellowship. This research developed computational methods to understand the nanoscale structural characteristics, energy levels, couplings, and related parameters for DNA-scaffolded molecular networks. Three methods are described: (1) a genetic algorithm approach to deduce the structures and Hamiltonians of molecular networks; (2) an approach based on the hierarchical equations of motion to calculate the vibronic dynamics and corresponding heat currents, which impact quantum-mechanical dephasing in these systems; (3) a Random Forest machine-learning algorithm to analyze the roles of particular molecular arrangements on the functional energy-transport processes. These methods collectively reveal the structure-dynamics-function relationships in DNA-scaffolded molecular networks, which is an important step toward optimizing these materials for uses such as quantum-mechanical technology or light-harvesting materials.

This page intentionally left blank.

Computational Methods for Determining Structure and Dynamics in DNA-Scaffolded Molecular Networks

Introduction

For over 3 billion years,[1] nature has developed pigment-protein complexes with well-optimized optoelectronic functions that involve complex, efficient processes.[2] In comparison, these feats have not yet been matched in artificial materials.[3] The optoelectronic functions in natural systems include optimized processes like highly efficient energy transport, complicated mechanisms like those in water oxidation, and mechanisms involving strong nuclear-electronic interactions like photoprotection. [2, 4-5] These functions occur within the electronic degrees of freedom of these systems, which are typically the electronic or vibronic states of their embedded molecular networks. These natural systems indicate that repeating monomer units can generate this strong performance.[2] As a result, the functions are dictated by the aggregation characteristics of the monomers. In contrast, for artificial systems, synthetic chemical modifications are often used to tune functional behaviors, often without much control of the aggregate structure.

Quantum mechanical excitations are described by both an amplitude and phase component.[6] When a superposition of these states is excited by coherent light, such as that from a laser, the excitations are also generated in-phase. By definition, coherent dynamics occur when the components of this superposition maintain a well-defined phase relationship as they propagate. Measurements of coherent electronic motion in photosynthetic proteins[7-8] have revealed the that scaffolded molecular systems can exhibit coherent electronic dynamics on similar time scales to their energy-transport times,[8] which implies that the coherent motion engages in the energy-transfer dynamics. These results are relevant to applications such as solar-energy harvesting, or more challenging interests such as quantum information technologies.[9] Though the biological fitness of natural systems may not depend on these quantum-mechanical effects,[10] artificial molecular systems can still use quantum mechanical phenomena to perform useful quantum functions in fields such as cryptography, sensing, measurement, photovoltaics, and computation.[11-12]

Systems that are usually considered for quantum technologies include optical cavities,[13] trapped ions,[14] spins,[15] nitrogen vacancies,[16] and superconductors.[17] These systems are largely inorganic materials, photonic systems, diamond lattices, or atomic condensates. In comparison, the electronic states of organic systems are not typically considered strong substrates for quantum technologies that require long-lived coherences like universal quantum computers. The reason is that their electronic dephasing rates are typically fast compared to analogous processes in these other systems. However, the dephasing rates only need to be slow relative to the electronic phase evolution and energy-transport, which can also be very fast in organic systems compared to these other media.[18] Organic molecules are subject to large, thermalized nuclear motions which increases their dephasing rates compared to these other systems.[19] Put differently, these molecules are more strongly coupled to their environmental baths than many of these other systems. Dephasing arises from dissipation of energy and quantum information from the system to its environment, as well as stochastic perturbations of the states that disrupt their phase relationships.[6] In the chemical physics, these behaviors are expressed within

---

Manuscript approved November 21, 2022.

the Hamiltonian and corresponding system-bath interactions. The Hamiltonian describes the average couplings and energies of the system, while perturbations from these average values are described by the system-bath interactions.

In order to gain control of these processes so that they can be optimized, first we need the following: (a) methods to understand the nanoscale configurations of N-Site (N>1) heterogeneous systems, such as their molecular positions and orientations, and the corresponding Hamiltonian and system-bath interactions; (b) methods to compute their electronic dynamics based on these parameters, including the quantum-mechanical phase evolution; (c) methods to understand the system-bath dynamics; and (d) methods to assign the contributions of individual monomer Sites to bulk functions in large systems, where computations are difficult due to their computational expense. Here, the methods that were developed in all four of these areas will be described, and their results will be discussed.

These respective methods accomplish the following: (a) To understand the nanoscale configurations of N-Site heterogeneous systems, genetic algorithm methods were developed that use physical models to calculate the linear absorption and circular dichroism spectra, and optimize the nanoscale characteristics in comparison to the corresponding measured spectra. (b, c) The electronic dynamics are calculated using the hierarchical equations of motion (HEOM), including methods that compute the energy transport between the system and bath. (d) Larger systems were addressed using a combination of experimental measurements, machine-learning methods, and computational modeling of subsets of the whole system. Using these methods, the roles of individual Sites and couplings on energy transport can be determined, and mapped to parameters like their positions, orientations, and chemical compositions.

Methods

Genetic algorithms. The details of the genetic algorithm method were described in detail previously,[20] but a summary will be provided here. Genetic algorithms are a stochastic optimization method, where the system is funneled toward the correct solution by stochastic optimization steps. The goal of this approach is to determine the optimal nanoscale parameters from the experimental linear absorption and circular dichroism measurements. These parameters include the monomers' positions, orientations, electronic transition energies, vibrational energies, system-bath coupling, and site-to-site electronic energy offsets. The reasons for using this approach are the following. First, even subtle changes in the parameters can lead to large differences in the calculated spectra. Second, the number of parameters can be quite large. For example, a two-Site homogeneous system uses 8 input parameters and generates an 18 x 18 Hamiltonian. In comparison, a three-Site heterogeneous system expands to 18 input parameters and an 81 x 81 Hamiltonian. Therefore, genetic algorithms are used with a Delaunay clearing protocol. Clearing protocols ensure that the search spans the search space broadly, rather than becoming focused on a local optimum that may not be the global optimum. Furthermore, Delaunay triangulation is used to project the search to empty regions of the search space.[21]

A flow chart for the genetic algorithm is shown in Figure 1. First, an initial guess is used, which contains information such as the positions, transition dipole angles, electronic and vibrational energy levels, and electronic energy offsets of the monomers within the network. Second, guesses are generated by randomly perturbing the guess parameters, to create 1000 distinct guess sets. Third, each of these guess sets is used to generate a Hamiltonian, which is then used to calculate linear absorption and circular dichroism spectra. Fourth, the calculated spectra are compared to measured spectra to generate a score. Subsequently, the scores are used to generate a next generation of guesses, including occasional random variations ("mutations") of the individual values. Using this new set of guesses, the process repeats. At first, the mutations occur with a large range, representing a coarse optimization. However, as the algorithm proceeds without increases in the score, this range sequentially narrows to represent a more fine-grained search. This range sequentially narrows from 500 to 100, 10, 3, 1, 0.4, 0.1, 0.01, and 0.001.

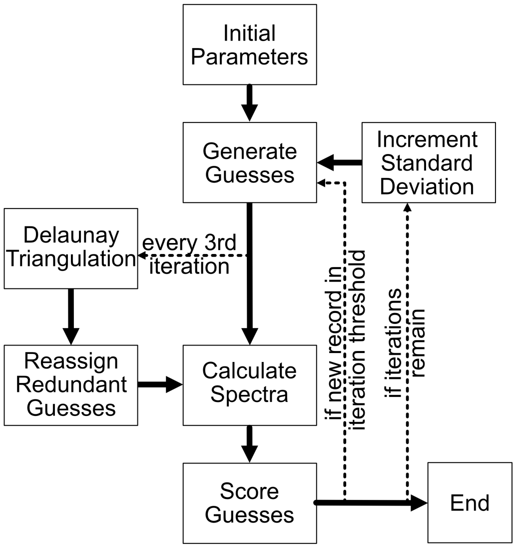

Figure 1. A flow chart for the Genetic Algorithm. The starting position is the "Initial Parameters" box. Solid arrows indicate the standard flow, while dotted lines indicate conditional paths.

Scores were obtained by comparison of the calculated and measured linear absorption and circular dichroism spectra, as well as their first derivatives. This comparison was made by obtaining the sum of the difference-squared between the calculated and experimental spectra. These terms $f_{k,i}$ (where i spans 1 to 4 and is the index counting the absorption or circular dichroism spectra and their first derivatives) were then input into the cost function (equation 1) to obtain a score for the k^{th} guess within the generation.

$$F_k = \frac{1}{\prod_{i=1}^{4} f_{k,i}} \sum_{i=1}^{4} \frac{1}{f_{k,i}} \quad \text{(equation 1)}$$

The selection of parents for the subsequent generation was performed by assigning a probability to each member of the previous generation (equation 2) based on its score, and then selecting pairs of parents at random based on these probabilities. These parents were then used to parametrize each guess of the next generation, with a 50% chance of inheriting each parameter from each parent. Subsequently, these inherited parameters were occasionally assigned a mutation at random, according to the method described above.

$$P(k) = \frac{F_k}{\sum_{j=1}^{200} F_j} \qquad \text{(equation 2)}$$

Spectral calculations. The spectral calculation method used for the genetic algorithm is a semiclassical method, which was selected for its relatively low computational cost compared to the HEOM method described subsequently. Because the genetic algorithm performs potentially millions of these calculations in a typical run, speed is an important factor in the algorithm's usefulness. The spectral calculations for monomers and homogeneous dimers were described in detail in a previous publication.[20] Here, the method has been extended to heterogeneous systems, and systems with more than two monomer Sites. The vibronic Hamiltonian is described by equation 3. This Hamiltonian's vibronic basis vectors $|\tilde{n},\tilde{v}\rangle$ are defined by the tensor product of the electronic and vibrational states (equation 4). Here, $\tilde{n}$ and $\tilde{m}$ describe the electronic configuration, $\tilde{v}$ and $\tilde{l}$ describe the vibrational configurations, $O(\tilde{n})$ is the electronic energy offset, and $J_{\tilde{n},\tilde{v},\tilde{m},\tilde{l}}$ is the vibronic coupling. The generalized vector $\tilde{n}$ is used to discuss networks with an arbitrary number of Sites. In the limit of a monomer system, for instance, $\tilde{n}$ can be replaced by a scalar Site index n.

$$\hat{H} = \sum_{\tilde{n},\tilde{v}} E_{\tilde{n},\tilde{v}}|\tilde{n},\tilde{v}\rangle\langle\tilde{n},\tilde{v}| + O(\tilde{n}) + \sum_{\tilde{m}\neq\tilde{n},\tilde{l}} J_{\tilde{n},\tilde{v},\tilde{m},\tilde{l}}|\tilde{n},\tilde{v}\rangle\langle\tilde{m},\tilde{l}| \qquad \text{(equation 3)}$$

$$|\tilde{n},\tilde{v}\rangle = |\tilde{n}\rangle \otimes |\tilde{v}\rangle \qquad \text{(equation 4)}$$

The vibronic coupling is described by equation 5. Here, an extended dipole model is used, rather than a more often-used point-dipole approximation. The reason is that the point-dipole approximation fails for short intermolecular distances, while the extended dipole model is more well-behaved in this limit.[22] In the extended dipole model, the polarization generated by the interaction between the light and electronic charge density is described by a pair of positively and negatively charged point charges positioned on opposite sides of the molecule along its transition dipole vector. $C_{\tilde{n},\tilde{m}}$ is the Coulombic coupling (equation 6) between electronic states $\tilde{n}$ and $\tilde{m}$, and r_α^+ or r_α^- represent the positions of the positive or negative partial charges respectively for molecule α (out of the total quantity of molecular sites A). The charge $q_{\tilde{n}}$ is defined in equation 7, ϵ_0 is the permittivity in free space, e is the elementary charge, $\mu_{\tilde{n}}$ is the electronic transition dipole strength, and $L_{\tilde{n}}$ is the length of the molecule in the direction of the electronic transition dipole. $F_{v,l}$ is the Franck-Condon factor between the vibrational states v and l (equation 8), $\tilde{g}$ is the ground vibrational state, S is the Huang-Rhys factor (equation 9), γ is the Stokes shift, and ΔE_v^{est} is the estimated vibrational energy gap.

$$J_{\tilde{n},\tilde{v},\tilde{m},\tilde{l}} = F_{\tilde{g},\tilde{v}}F_{\tilde{g},\tilde{l}}C_{\tilde{n},\tilde{m}}\left(\sum_{\alpha=0}^{A}\frac{1}{|r_\alpha^+ - r_\alpha^-|} - \sum_{\beta\neq\alpha}^{B}\frac{1}{|r_\beta^+ - r_\beta^-|}\right) \qquad \text{(equation 5)}$$

$$C_{\tilde{n},\tilde{m}} = \frac{q_{\tilde{n}}q_{\tilde{m}}}{4\pi\epsilon_0} \qquad \text{(equation 6)}$$

$$q_{\tilde{n}} = \frac{e\mu_{\tilde{n}}}{L_{\tilde{n}}} \qquad \text{(equation 7)}$$

$$F_{v,l} = exp\left(\frac{-S}{2}\right)\sum_{\eta=0}^{v}\sum_{\xi=0}^{l}\frac{(-1)^\xi}{\eta!\xi!}\sqrt{\frac{S^{(\eta+1)}v!l!}{(v-\eta)!(l-\xi)!}} \text{(equation 8)}$$

$$S = \left(\frac{\gamma}{2\Delta E_v^{est}} + \frac{1}{4}\right) + z \qquad \text{(equation 9)}$$

After the Hamiltonian is determined, the linear absorption and circular dichroism spectra are calculated. When pulsed light passes through the system, its electric field momentarily interacts with the sample's electronic charge density, which exerts a force that pushes the positive holes and negative electrons in opposite directions along its transition dipole. After the light is gone, the system is polarized, and this polarization oscillates along its transition dipole until it eventually emits or otherwise dissipates its energy and returns to its ground state. In the absence of environmental perturbations, these oscillations occur at the resonant angular frequency ω_α for state α, however perturbations cause the phase evolution to deviate according to a lineshape function $g_\alpha(t)$ (equation 10), whose effect is to contribute line-broadening to the corresponding optical spectra. The term P_α stands for the oscillator strength P_α^{osc} (equation 11) for linear absorption spectra, or rotational strength P_α^{rot} (equation 12) for circular dichroism spectra. Fourier transforms are used to convert this time-domain signal to the frequency-domain spectrum. μ_α is the transition dipole magnitude, $c_{a,\alpha}$ is the overlap between Site a and state α, and $r_{a,b}$ is the distance between Sites a and b. The angular brackets account for static energy disorder, which occurs due to non-uniform individuals within the sample ensemble. These brackets are accounted for by convoluting the contents to a Gaussian function.

$$\varrho(t) = \sum_\alpha^A P_\alpha exp\left(-i\omega_\alpha t - g_\alpha(t)\right) \quad \text{(equation 10)}$$

$$P_\alpha^{osc} = \langle \left|F_{0,\alpha}\mu_\alpha\right|^2 \rangle \quad \text{(equation 11)}$$

$$P_\alpha^{rot} = \langle \sum_a \sum_{b>a} c_{a,\alpha} c_{b,\alpha} F_{0,a} F_{0,b} \left(r_{a,b} \cdot (\mu_a \times \mu_b)\right) \rangle \quad \text{(equation 12)}$$

Hierarchical equations of motion. Many methods exist to calculate the quantum mechanical evolution of an excited system, like the one described in the previous section. A major distinguishing factor in these methods is the approximations they take, with respect to the system and bath interactions. In the extremes where the intrasystem coupling is strong compared to the system-bath coupling, or vice versa, the Redfield or Förster theories are applicable, respectively. Redfield theory captures the quantum mechanical evolution of the system when the impact of the bath is small, while Förster theory primarily focuses on the evolution of the bath and the thermodynamic consequences of the bath relaxation on the system. HEOM explicitly keeps track of the system and bath configurations within a quantum-mechanical formalism, allowing it to interpolate between these extremes at the cost of higher computational expense. This range is necessary because the algorithm may place the chromophores far apart or close together, which can correspond to the Förster or Redfield conditions respectively, and yet it would be desirable to be able to make an apples-to-apples comparison for the dynamics throughout this range.

HEOM has been described previously,[23-25] but it will be summarized here. The total system is assumed to be separable into three components: the electronic contribution, environmental bath contribution, and system-bath coupling. The Hamiltonian is therefore composed by the sum these three parts (equation 13). The System Hamilotonian $\widehat{H}_s$ is defined by the electronic Site transition energies E_n and reorganization energies λ_n for Site n, as well as the vibronic couplings V_{nm} between Sites n and m (equation 14). Meanwhile, the environmental bath Hamiltonian $\widehat{H}_e$ adopts a harmonic oscillator model, which depends on the momentum $\hat{p}_{nj}$ and position $\hat{x}_{nj}$ operators and vibronic angular frequency ω_{nj} (equation 15). The system-bath coupling $\widehat{H}_{se}$ is shown in equation 16.

$$\widehat{H}_{tot} = \widehat{H}_s + \widehat{H}_e + \widehat{H}_{se} \quad \text{(equation 13)}$$

$\hat{H}_s = \sum_n^N (E_n - \lambda_n)|n\rangle\langle n| + \sum_{m\neq n}^N V_{nm}|n\rangle\langle m|$ (equation 14)

$\hat{H}_e = \frac{1}{2}\sum_n^N \sum_j^\infty \frac{\hat{p}_{nj}^2}{m_{nj}} + m_{nj}\omega_{nj}^2\hat{x}_{nj}^2$ (equation 15)

$\hat{H}_{se} = \sum_n^N \sum_j^\infty c_{nj}\hat{x}_{nj}|n\rangle\langle n|$ (equation 16)

For the system modeled here using this method, the monomers were several nanometers apart and therefore the point-dipole approximation was used to find the vibronic coupling between the Sites (equation 17). Here, κ_{nm} is the orientation factor (equation 18), μ_n is the transition dipole (equation 19), n_0 is the index of refraction (which was set to 1.333, which is the value in water at room temperature), n_0^2 approximates the dielectric constant (along with a component included into the scalar term in front of equation 17),[26-27] and $\vec{R}_{nm}$ is the displacement between Sites n and m. Furthermore, $\vec{r}_n$ is the unit vector for the displacement, c is the speed of light, $\tilde{\omega}$ is the weighted average of the absorption spectrum's frequency, and $\epsilon(\omega)$ is the extinction coefficient.

$V_{nm} = (5.035 \cdot 10^3)\frac{\kappa_{nm}\mu_n\mu_m}{n_0^2|\vec{R}_{nm}|^3}$ (equation 17)

$\kappa_{nm} = \vec{r}_n \cdot \vec{r}_m - 3(\vec{r}_n \cdot \vec{r}_{nm})(\vec{r}_m \cdot \vec{r}_{nm})$ (equation 18)

$\mu_n = \sqrt{\frac{4.319\cdot 10^{-9}\cdot 3\hbar e^2}{4\pi c m_e \tilde{\omega}}\int d\omega \epsilon(\omega)}$ (equation 19)

The bath was modeled using a Brownian multimode oscillator model, allowing the system-bath coupling $V_{se}(\omega)$ to be modeled using the Drude-Lorentz spectral density (equation 20). Here, λ was the nuclear relaxation rate, which was set to 10 ps^{-1} in correspondence to other organic chromophore networks.[28-29] Because the calculations assumed a temperature of 298 K, the low-temperature correction was not included in the computation.[28]

$V_{se}(\omega) = \frac{2\lambda\gamma\omega}{\omega^2+\gamma^2}$ (equation 20)

Using the system-bath coupling, the correlation function $C_j(t)$ for the collective bath operator is calculated (equation 21). The independent bath assumption was applied, so each vibronic state was assigned its own bath.

$C_j(t) = \frac{1}{\pi}\int_{-\infty}^{\infty} d\omega V_{se}(\omega)\frac{e^{-i\omega t}}{1-e^{-\beta\hbar\omega}}$ (equation 21)

Because the correlation function is difficult to compute in this form, it was recast using Matsubara frequencies v_k and their coefficients a_k (equations 22-26). The expansion into Matsubara frequencies extends to infinite terms, however a reasonable approximation is obtained when a hierarchy cut-off function K is applied (here, it is set to 2).[28, 30] This approximation is equivalent to the 2K^{th} order in perturbation theory.[31] Here, $\beta = \frac{1}{k_BT}$ with the Boltzmann constant k_B and temperature T. The terminator contributions for orders above K are then added after applying the Markovian approximation.[25, 32]

$C_j(t > 0) = \sum_k^K a_k e^{-v_k t}$ (equation 22)
$a_{k=0} = \frac{\lambda\gamma}{\hbar}\left[cot\left(\frac{\beta\gamma}{2}\right) - i\right]$ (equation 23)
$a_{k>0} = \frac{4\lambda\gamma v_k}{\beta\hbar^2(v_k^2-\gamma^2)}$ (equation 24)
$v_{k=0} = \gamma$ (equation 25)
$v_{k>0} = \frac{2\pi k}{\beta\hbar}$ (equation 26)

Meanwhile, the evolution of the density operator $\hat{\rho}_n$ was computed using equations 27-28.[25, 30, 32-33] Here, n_{jk} is a non-negative index spanning the electronic states $1 \geq j \geq N$ and Matsubara expansion terms $0 \geq k \geq \xi$, where N is the number of vibronic states and ξ was set to 1. Also, $n_{jk}^{\pm} = n_{jk} \pm 1$, except negative indices were set to zero. The scaling of this master equation was discussed in more detail previously.[33] The Quantum Toolbox in Python (QuTiP) library was used for the HEOM calculations.[34-35]

$$\frac{d}{dt}\hat{\rho}_n = \frac{-i}{\hbar}[H_s, \hat{\rho}_n] - \sum_{j=1}^N \sum_{k=0}^{\xi} n_{jk} v_k \hat{\rho}_n - i\sum_{j=1}^N \sum_{k=0}^{\xi} \sqrt{(n_{jk}+1)|a_k|}\left[\hat{P}_j, \hat{\rho}_{n_{jk}^+}\right] -$$
$$\sum_{j=1}^N \left(\sum_{m=\xi+1}^{\infty} \frac{a_m}{v_m}\right)\left[\hat{P}_j, \left[\hat{P}_j, \hat{\rho}_n\right]\right] - i\sum_{j=1}^N \sum_{k=0}^{\xi} \sqrt{\frac{n_{jk}}{|a_k|}}\left(a_k \hat{P}_j \hat{\rho}_{n_{jk}^-} - a_k^* \hat{\rho}_{n_{jk}^-} \hat{P}_j\right) \quad \text{(equation 27)}$$
$\hat{P}_j = |j\rangle\langle j|$ (equation 28)

Next, this method is used to calculate the heat current between the system and its baths. These calculations result in the quantum heat currents from the perspective of the system j_S^K (equation 29) or bath j_B^K (equation 30), while $A_k(t)$ is specified by equation 31.[36-37] Because the baths coupled to each vibronic state are assumed to be independent from one another, the interbath interaction terms were omitted from equation 30.[36] These dissipation effects are important for the dephasing characteristics in these systems, which also impact the systems' quantum dynamics. In equations 29-30, j (out of max J) is the index for the auxiliary density operator in HEOM, which specifies the configuration of each bath mode. The terminator component Δ_k that is approximated by the Markovian approximation is obtained, following the work by Ishizaki and Tanimura.[25, 32] The imaginary component of the correlation function at time-zero is denoted by $C_k^I(0)$. The coupling between the system and each bath is denoted by $\hat{V}_k$. All of these terms are available within an HEOM calculation.[36]

$j_S^K = -\sum_j^J Tr\{A_k(t)\hat{\rho}_j(t)\} + \frac{i}{\hbar}\Delta_k Tr\{[A_k(t), \hat{V}_k]\hat{\rho}_j(t)\}$ (equation 29)
$j_B^K = \frac{d}{dt}\langle H_B^K\rangle = \sum_j^J \gamma_{k_j} Tr\{\hat{V}_k \hat{\rho}_j(t)\} + \frac{2}{\hbar}C_k^I(0)Tr\{\hat{V}_k^2\hat{\rho}_j(t)\} + \frac{i}{\hbar}\Delta_k Tr\{[A_k(t), \hat{V}_k]\hat{\rho}_j(t)\}$
(equation 30)
$A_k(t) = \frac{i}{\hbar}[\hat{H}_S(t), \hat{V}_k(t)]$ (equation 31)

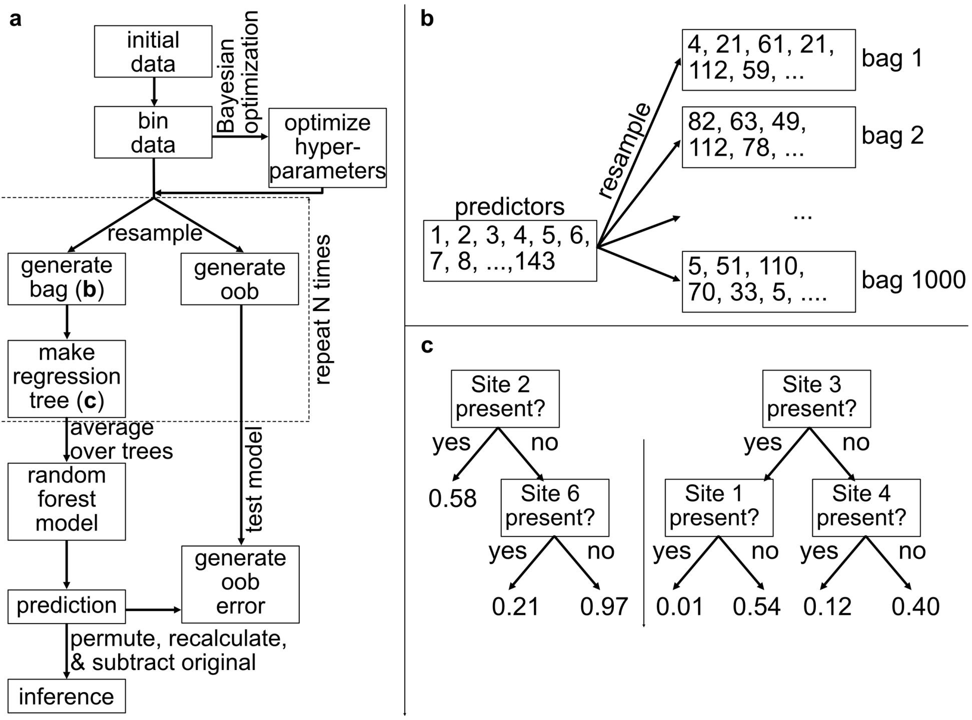

Figure 2. (a) A schematic showing the Random Forest algorithm. (b) An example of resampling. (c) An example of binary regression trees.

Random Forest machine-learning algorithm. The Random Forest algorithm was described previously,[38-39] however it is summarized here. This algorithm is useful when the goal is to map input parameters to output values, for some collection of measurements. The premise of this algorithm is to develop a series of weak predictions based on subsets of the existing data, and to average these weak predictions together in order to generate a stronger prediction overall. It has numerous advantages, such as a natural resistance to overfitting, no dependence on a posited physical model, scalability to large data sets, a natural tabulation of non-linear variable dependencies (ie., when the input variables depend on each other), and well-established validation methods.[38]

The Random Forest method generates a set of short binary regression trees that describe aspects of the data set, and then averages their predictions to produce a predictive model. The algorithm is described in Figure 2a. The initial data are comprised of input parameters and their corresponding output values. In this case, the input values are Booleans for each Site, indicating whether it is present or absent from the system. The output values are the FRET efficiencies. The data are binned and Bayesian optimization is used to determine the optimal hyperparameters for the machine-learning method. The hyperparameters are the minimum number of observations per terminal node (a.k.a. the “minimum leaf size”), the maximum number of splits in the binary trees, and the quantity of predictors (data points) selected. The data are then resampled, as shown in Figure 2b for an example with 143 data points. The resampled bootstrap aggregates (known in the machine-learning field as “bags”) are then used to produce binary trees, as shown in Figure 2c. The out-of-bag (oob) component, containing all the predictors that were not selected during the selection process, are “new measurements” from the perspective of the model and therefore used to test its ability to predict new measurements. This algorithm used the Matlab TreeBagger and Bayesopt algorithms.

The importance of each input parameter is inferred by building a subsequent Random Forest model and subtracting its predictions from those of the first model. The difference in this subsequent model is that a single input parameter is randomly redistributed across the predictors, effectively breaking its correlation to the output values, while still retaining the data set’s overall statistics so that apples-to-apples comparisons can be made across the two models.[38] In practice, every model is produced ten times and averaged, to reduce the statistical variations. When this inference approach is performed for an input parameter, its Linear Variable Importance (LVI) is obtained. The LVI describes how significant that input parameter is for determining the output values. If randomly scrambling the input parameter does not significantly change the model predicts, then the LVI is low and the parameter is not very relevant for the underlying processes. However, if the model predictions change significantly when the input parameter is randomly scrambled, then that parameter must be important. Likewise, by subtracting the LVI in the presence of a second Site, from the LVI in the absence of that second Site, the Nonlinear Variable Importance (NVI) between these two Sites is obtained.

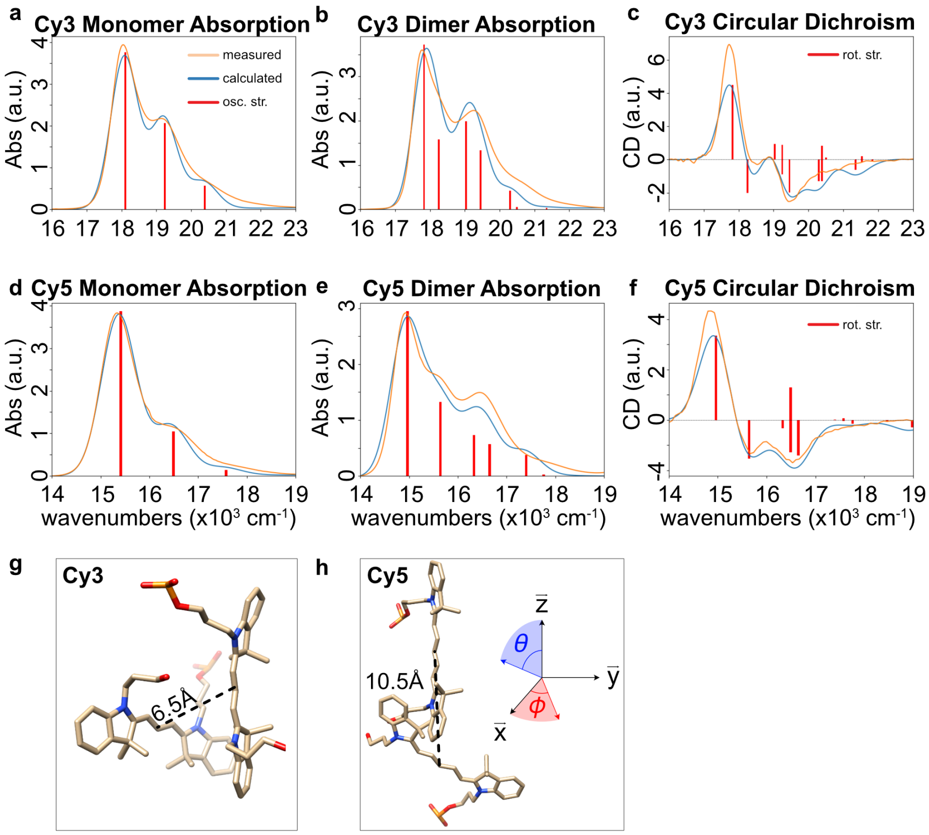

Figure 3. The genetic algorithm method was used to obtain nanoscale parameters for Cy3 (a-c) and Cy5 (d-f) dimers. The results aggregation characteristics are shown in figures g-h. The corresponding parameters are shown in Table 1.

The NVI describes cooperative (if positive-valued) or inhibiting (if negative-valued) effects between input parameters.

Results

Genetic algorithms. Initially, the genetic algorithm approach was only valid for homogeneous dimer systems.[20] First, these are shown as a starting point. Two different DNA-scaffolded dye systems were synthesized, containing either Cyanine-3 (Cy3) or Cyanine-5 (Cy5) monomers. Their linear absorption and circular dichroism spectra were measured, as well as those of the corresponding DNA-monomer systems. For the corresponding spectroscopic calculations, the temperature was assumed to be 298 K, and the cut-off frequency of the Ohmic spectral density was assumed to be 200 cm^{-1}. The transition dipole moments for Cy3 and Cy5 were 12.8 and 13.4 D, respectively. For the Delaunay triangulation in these calculations, only the highest-scoring 100 members were considered, and four degrees of freedom were considered at a time per iteration (randomly selected). The reassignment threshold was set to 10^{-10}, which was intended to reassign near-duplicates only. Using these parameters, the results are shown in Figure 3, and the resulting nanoscale parameters were obtained (Table 1).

The parameters in Table 1 describe the relative positions and orientations of the monomers within the dimer system, as well as their optical gap, vibrational spacing, and static inhomogeneous broadening. Note that this method distinguishes the static inhomogeneous broadening contribution, which may arise from static or effectively static polydispersity within the sample ensemble, from the dynamic inhomogeneous broadening and homogeneous broadening contributions that arise from the electronic-nuclear interactions. More information is available in a previous publication.[20]

Subsequently, the algorithm was expanded to accommodate both heterogeneous molecular networks, as well as those that contain more than two Sites. For heterogeneous networks, two assumptions were relaxed. The first is that some of the parameters, such as the optical gap and vibrational spacing, were no longer assumed to be identical for each monomer. The impact of this change was to increase the number of optimization parameters. Secondly, a zero-energy offset was applied to account for different ground-state energies in the distinct monomers. Meanwhile, to expand the computation to more than 2 Sites, much of the physics

Table 1. The difference in inclination angle (θ), azimuthal angle (ϕ), and position coordinates (x, y, z) are shown, as well as the optical gap ($\boldsymbol{E_{0-0}}$), vibrational spacing ($\Delta\boldsymbol{E_v}$), and peak broadening half-width at half-maximum (HWHM).

	Cy3	**Cy5**
$\boldsymbol{\theta}$ (deg.)	99.3	104.6
$\boldsymbol{\phi}$ (deg.)	8.27	87.4
$\boldsymbol{x}$ (Å)	-6.3	-2.9
$\boldsymbol{y}$ (Å)	-0.9	-4.6
$\boldsymbol{z}$ (Å)	-1.5	-9.0
$\boldsymbol{E_{0-0}}$ (cm^{-1})	18104	15412
$\Delta\boldsymbol{E_v}$ (cm^{-1})	1144	1082
HWHM (cm^{-1})	126	135

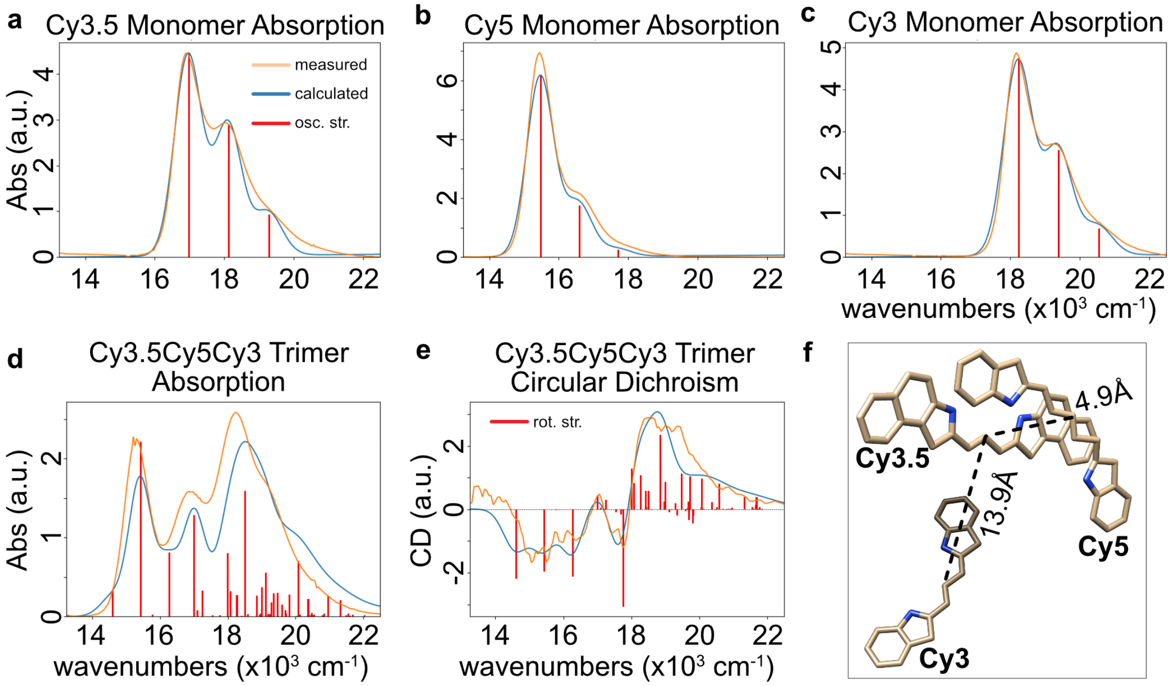

Figure 4. (a-e) The absorption and circular dichroism spectra of the DNA-scaffolded Cy3.5Cy5Cy3 trimer system are shown, as well as the constituent monomers' spectra. (f) The aggregate structure of the trimer system is shown, as obtained by the genetic algorithm.

had to be generalized to accommodate variably sized Hamiltonians and other parameters, and some of the parameters had to be expanded into Cartesian products to scale properly. Because the computational cost also increased from these changes, substantial work was put into speeding up the algorithm, by making the code more efficient, improving the parallel processing, and converting to Python-wrapped c or machine language by using Cython or Numba just-in-time compiling ("jitting") methods, respectively and as appropriate. The code was also made receptive to GPU computation. The result was approximately a 50x speed-up. Overall, these changes required a substantial rewriting of thousands of lines of code.

The improved algorithm was used on a three-site, heterogeneous system. This system was composed of Cyanine-3.5 (Cy3.5), Cy5, and Cy3. The results for the monomers' linear absorption spectra and trimer's linear absorption and circular dichroism spectra are shown in Figure 4. By comparing the dimer spectra in Figure 3 with the trimer spectra in Figure 4, it is apparent by the larger quantity of red bars in Figure 4 that there are many more states, and corresponding optical transitions, involved. Generally speaking, in the vibronic model, even considering only 3 electronic states containing 3 vibrational sub-levels each is enough for the blue edge of the spectrum to encompass a very large number of overlapping spectral peaks. As a result, it should not be attempted to judge peak widths, electronic couplings, transition frequencies, or similar parameters from the bluer peaks without a physical model like the one used here. This increasing complexity compared to the dimer model also explains why it is difficult to get as precise coincidence between the computed and measured spectra. Additionally, when more Sites are present, then more variations can exist in terms of defects,

Table 2. The inclination angle (θ), azimuthal angle (ϕ), and position coordinates (x, y, z) are shown, as well as the optical gap ($\boldsymbol{E_{0-0}}$), vibrational spacing ($\Delta\boldsymbol{E_v}$), and electronic energy offset (O).

	Cy3.5	**Cy5**	**Cy3**
$\boldsymbol{\theta}$ (deg.)	0	22.9	150.6
$\boldsymbol{\phi}$ (deg.)	0	63.2	56.9
$\boldsymbol{x}$ (Å)	0	4.8	5.2
$\boldsymbol{y}$ (Å)	0	-0.7	8.5
$\boldsymbol{z}$ (Å)	0	-0.6	9.8
$\boldsymbol{E_{0-0}}$ (cm^{-1})	16,982	15,486	18,245
$\Delta\boldsymbol{E_v}$ (cm^{-1})	1,158	1,116	1,157
O (cm^{-1})	0	-0.2	-1,432

where one or more of the Sites are missing in a small proportion of the samples. This polydispersity is not included in the model, but it could also explain some of the variations found between the computed and experimental spectra. Nonetheless, the model predicts a physically plausible configuration, in which the Cy3.5 and Cy5 are aggregated, while the Cy3 is more distant. The Cy3.5 and Cy5 have zero base-pair separation in the system, while the Cy3 does not, making this solution plausible. The nanoscale parameters for the trimer system are shown in Table 2. Note that Table 1 shows the difference in the angles and positions between the two monomers, because that reduces the number of parameters in the dimer system; while Table 2 shows their values, because there is no similarly easy simplification.

These results indicate that the vibrational mode is nearly unchanged, when comparing Cy3.5 and Cy3, at 1158 and 1157 cm^{-1}, respectively. Meanwhile, Cy5 has a vibrational frequency of 1116 cm^{-1}. This result indicates that the vibrational mode likely depends more on the chain bridging the two conjugated rings, than on the conjugated rings themselves. The Cy3.5 and Cy5 moieties have only a 0.2 cm^{-1} ground-state offset, while the Cy3 is more offset at 1432 cm^{-1}.

Hierarchical equations of motion. HEOM was used to calculate two systems. The first was a 14-Site DNA-scaffolded system whose structure was determined by MD simulations,[40] and the second was a trimer whose structure was deduced using the genetic algorithm method.

The 14-Site system was intended to be a molecular wire for energy transport, where the energy flows from a Donor end to an Acceptor end of its molecular network. This system was composed of two Donor Sites (Alexafluor 488 or AF488), followed by 10 Relay Sites (Cy3.5), and finally two Acceptor Sites (Alexafluor 647 or AF647). In order to understand the roles that the individual Sites played in this energy transport, the energy-transport dynamics were modeled using HEOM. The reason for using this more computationally expensive method, instead of other energy-transport models such as the Redfield and Förster models is that it, unlike these latter two models, HEOM interpolates between the extremes of stronger intra-network coupling or stronger system-bath coupling.[41] Because the systems under investigation are not guaranteed to be in either category, HEOM is used to take away the dependence on it.

The 14-Site Hamiltonian was computationally expensive to calculate, so the system was considered in terms of three subsets. The first five Sites, central ten Sites, and five last Sites

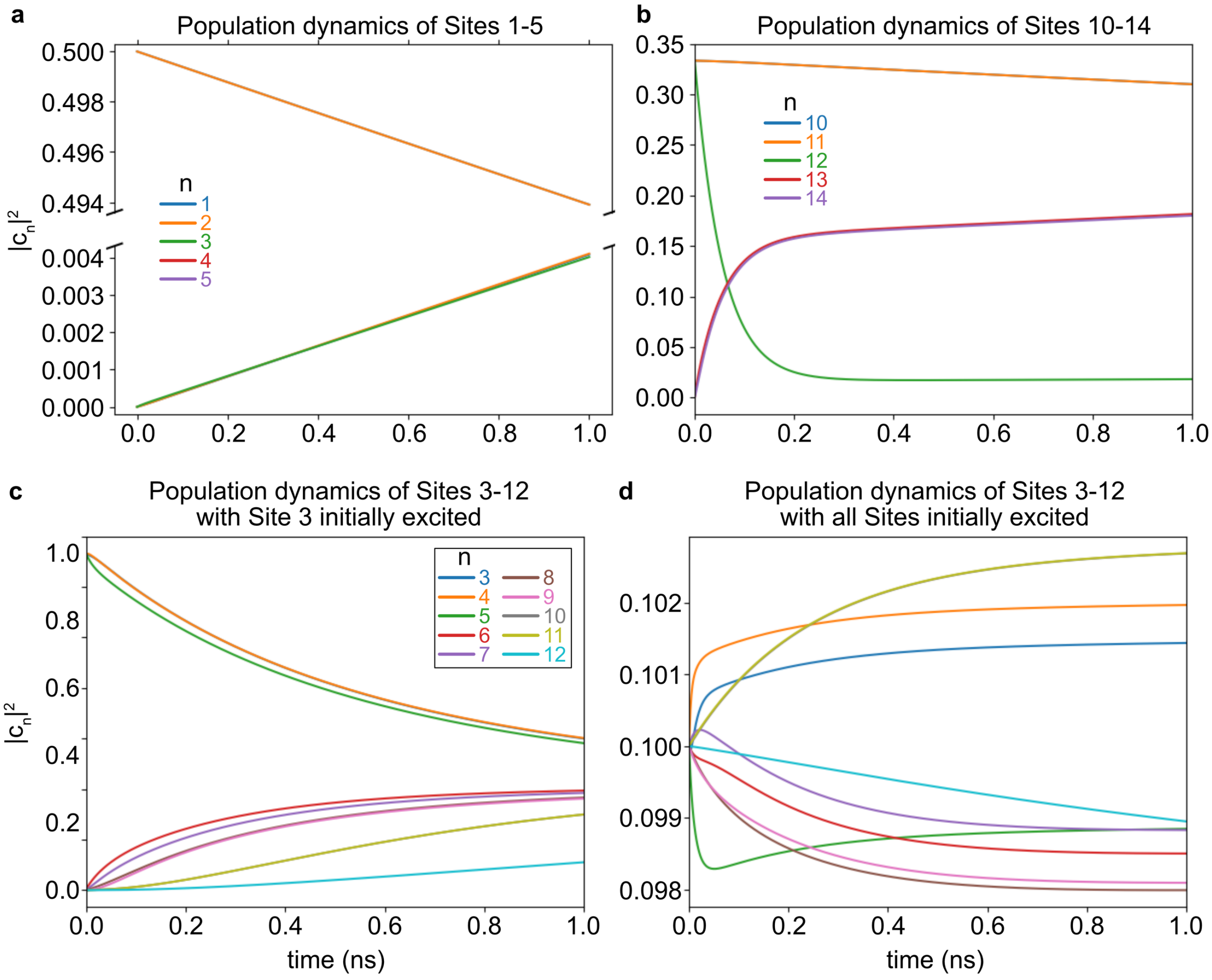

Figure 5. The electronic population dynamics are shown for the specified Sites (n), as calculated using HEOM. (a) The dynamics of the first five Sites within a 14-Site system are shown, containing two Donor monomers (1-2) and three Relay monomers (3-5). Sites 1-2 are initially populated. (b) The dynamics of the last five Sites are shown, containing three Relay monomers (10-12) and two Acceptor monomers (13-14). Sites 10-12 are initially populated. (c-d) The dynamics are shown when only Site 3 is initially populated (c) or when all of the Sites are initially populated (d). The transport across these various sub-sections of the molecular network are represented by these population dynamics.

were separately calculated. Note that some of the Relay Sites were computed twice using this approach. The first five Sites were important because they were composed of the two Donor sites, as well as the nearest three Relay Sites that could act as energy acceptors in an energy-transport process. Likewise, the last five Sites included three Relay Sites that could act as energy donors to the two Acceptor Sites. The Relay itself was calculated to assess transport across the long (10-Site) segment of homogeneous monomers. The dynamics resulting from these calculations are shown in Figure 5. Note that, because the monomers were spaced several nanometers apart, there are no oscillations indicative of coherent energy transport. These dynamics proceeded mainly by the Förster energy transport model.

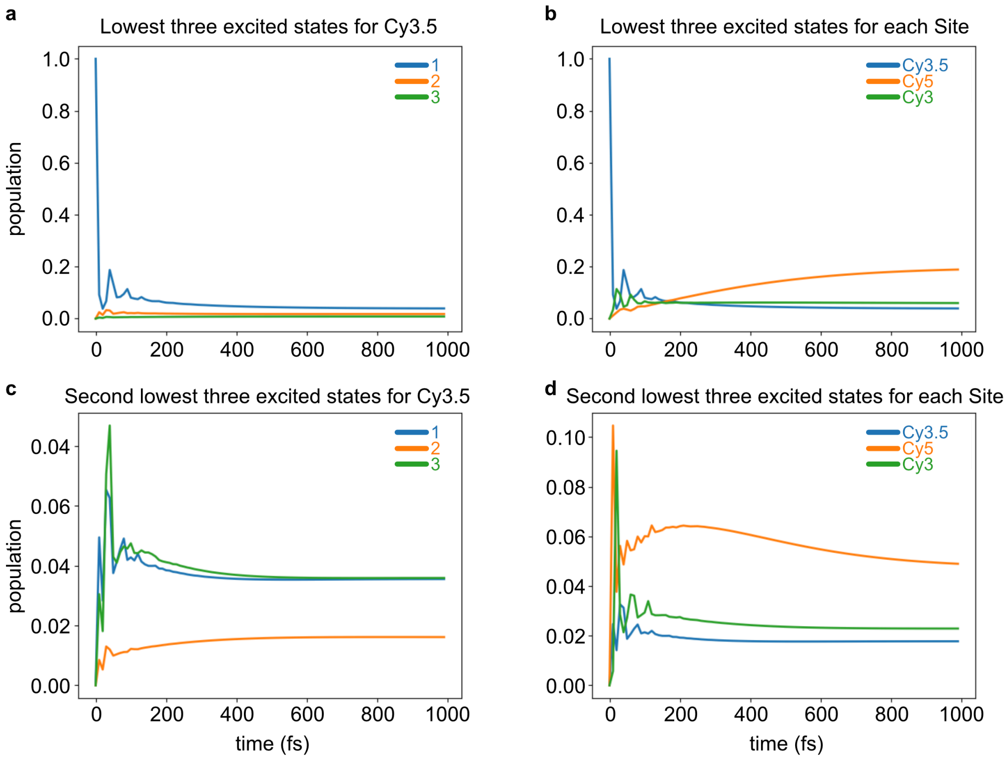

Figure 6. The population dynamics are shown for various subsets of the states for a 3-Site DNA-scaffolded molecular system.

Separately, the 3-Site system was investigated using HEOM. In this representative calculation, the Cy3.5 Site was initially populated. Its vibronic Hamiltonian contained 81 states, all of which participated in the population dynamics; but in the interest of brevity only a few subsets of the population dynamics are plotted here (Figure 6). The population dynamics are shown for the lowest vibronic state for each of the Sites, the second-fourth vibronic states, the lowest three vibronic states for Cy3.5, and the second-fourth states for Cy3.5.

Next, the heat currents are considered. These currents represent the energy transport dynamics between the chromophore system and its environmental bath, which are an important part of the quantum mechanical dephasing process. These results are available to HEOM, and unavailable to the Redfield and Förster models, because they involve quantum-mechanical entanglement between the system and its environmental bath states. Whereas these other models only treat the environment in a phase-averaged sense, which therefore averages out the quantum mechanical motion, HEOM retains the bath's phase information and therefore is capable of determining these quantum-mechanical heat currents. Following the methodology by Kato and Tanimura,[36] these currents are considered from the perspectives of the system energy, or the bath energy (Figure 7).

Random Forest Machine-Learning Algorithm. The Random Forest Machine-Learning Algorithm was used to investigate the contributions of individual Sites toward energy transport in a 14-Site DNA-scaffolded molecular network. Realistic functional materials will often require large molecular networks, however their complexity and computational cost increase with size.

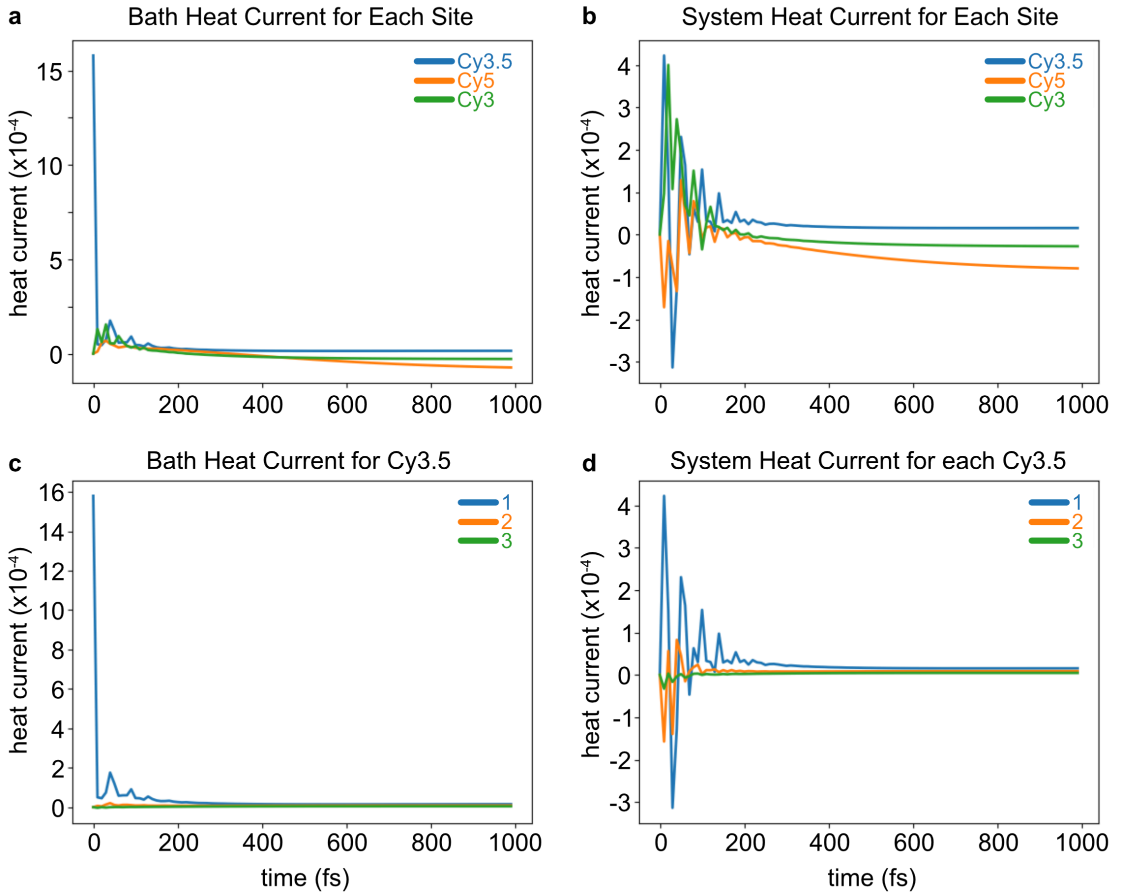

Figure 7. The bath (a, c) and system (b, d) heat currents are shown for the lowest vibronic state of all the Sites (a, b) and Cy3.5 alone (c, d).

Therefore, it becomes preferable to use experimental methods such as FRET measurements to understand their optimization rules. However, due to the complexity, machine-learning methods can recognize trends or patterns that unaided human observation can struggle to find. Furthermore, the modular nature of DNA-scaffolded systems allows systematic investigations. However, this process can be challenging when the variations have a non-trivial impact on the figures of merit, as is the case here with the impact of the molecular aggregation characteristics on the circular dichroism spectra for instance. Here, over 100 variations of the 14-Site system were made by removing zero or more Sites from the system. As the result, the eigenstates and eigenvectors of the system Hamiltonian were changed and the energy-transport efficiencies across the system varied in non-trivial ways. Therefore, machine-learning methods were used to understand the patterns within this big-data approach.

The linear Importance indicators of the various Sites were investigated, as well as their nonlinear Importances (Figure 8). Linear Importances are those that depend on the individual Sites without regard to the other Sites. In contrast, Nonlinear Importances describe cooperative or inhibiting effects that depend on clusters of Sites instead of just individual ones. Using these methods, three figures of merit were investigated. They were the Donor-quenching, Relay-quenching, and Wire-transfer efficiencies. These figures of merit coincide approximately with the sub-sections of the molecular network used to calculate the population dynamics in Figure 4. Likewise, the linear and nonlinear variable importances were obtained for the donor- and relay-quenching efficiencies (Figure 9).

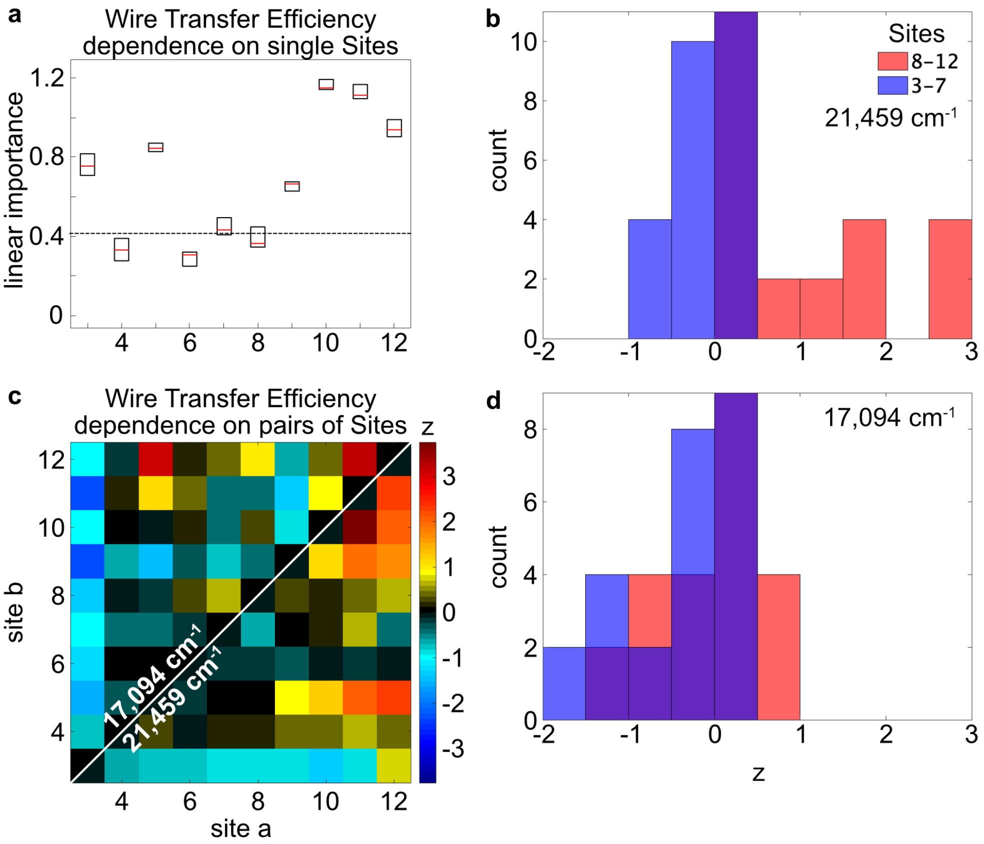

Figure 8. The dependence of the Wire Transfer FRET efficiency on the individual Relay sites is shown. (a) The linear variable importance is shown. (c) The nonlinear variable importance is shown, for when the Relay (17,094 cm^{-1}) or Donor (21,459 cm^{-1}) segments are excited. (b, d) Histograms are shown indicating the nonlinear variable importance of the indicated regions within the nonlinear variable importance 2D plot.

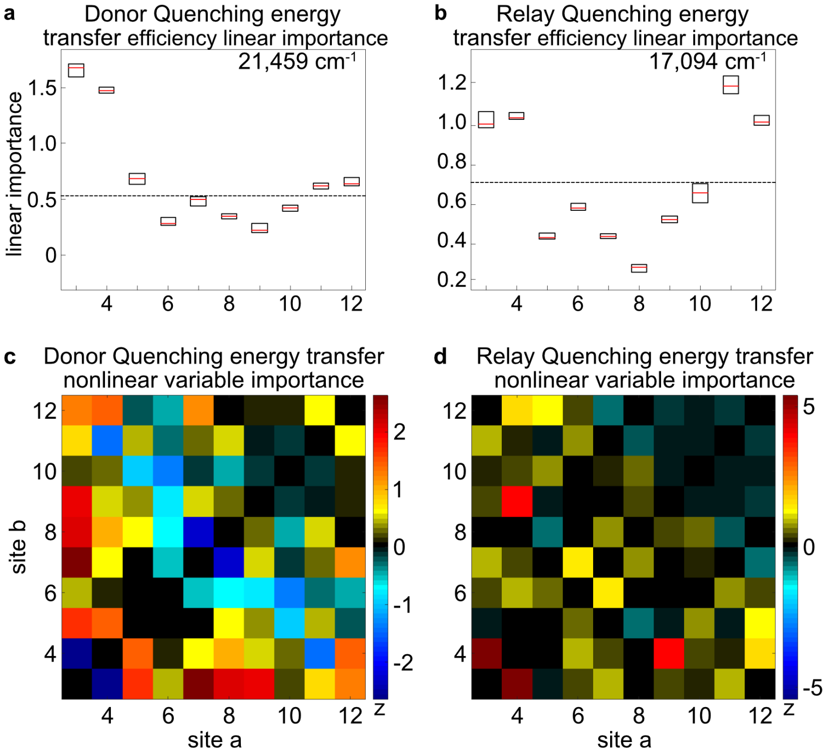

Figure 9. The linear (a, b) and nonlinear (c, d) variable importances are shown for the donor quenching efficiency (a, c) and relay quenching efficiency (b, d).

Discussion

The results focused on two systems, the 14-Site and 3-Site chromophore networks. The 14-Site system was intended to be a photonic wire, which transports energy from two initially photoexcited Donor Sites, through 10 Relay Sites, and finally into two Acceptor Sites.[40, 42] These Sites were arranged so that their excited-state potential energy surface allowed energy to flow downhill from the Donor to Acceptor Sites. While the detailed study of this system is contained in a manuscript currently submitted for publication,[40] the results are summarized here. The Random Forest analysis indicates that Sites 5 and 10-12 have cooperative effects that are important for energy transport. This result establishes that cooperative effects can take place over long distances, which in this case was as much as 20 nm and therefore too distant for direct energy transfer using a FRET mechanism. These cooperative effects are therefore indirect, where the energy originating on Site 5 eventually hops onto several Sites before reaching Sites 10-12. This analysis also indicated that Site 3 has an inhibiting interaction with most of the other Sites, which is likely due to its position furthest from the Acceptor Sites. It therefore provides a position that the population can reach through random walk or direct transfer from the Donor segment, which then has trouble percolating through the network to the Relay-Acceptor interface. Meanwhile, the Donor-quenching and Relay-quenching revealed a strong distance-dependence for direct energy transport from the Donor or Relay sites, respectively. However, especially in the case of the Donor-quenching results, there were cooperative interactions throughout the Relay Sites. These are difficult to explain, but may have to do with how the presence of these Sites mix to influence the vibronic eigenstates that are involved with the transport. Meanwhile, the HEOM results indicate that transport proceeds approximately equally from both of the Donor Sites, and that the Relay sites also accept the energy approximately equally, so that there is only a single transport channel. However, at the Relay-Acceptor interface, Site 12 is mainly involved with the energy transport to the acceptors. The other Sites therefore act cooperatively with Site 12, and influence the energy transport to Sites 13-14 mostly indirectly.

For the 3-Site system, the genetic algorithm was able to produce nanoscale parameters that could be used as inputs to produce the HEOM results. The aggregate structure obtained by the genetic algorithm made sense, because neighboring (0 base-pair separation) Sites were aggregated together, while the Site that was known to be more distant appeared distant in the genetic algorithm results as well. In the preliminary analysis of the HEOM results, the coherent dynamics are found to last for approximately 200 fs in both the system's population dynamics and heat currents. During this time, much of the signal decays as well for the initially populated vibronic state (State 1). Therefore, the vibronic coherences are present for the energy-transport dynamics in these systems, and the system is in a regime where the population motion can be controlled by coherent quantum-mechanical effects. The coherent heat exchange between the system and bath takes place for about 100 fs, as indicated by the oscillating pattern in the Bath Heat Currents. However, the coherences last about 200 fs in the System Heat Currents, suggesting that the coherences between the system and bath persist for about 100 fs, but that the system's coherences persist for twice as long among the other vibronic states in the system. These results establish that the heat currents in these DNA-scaffolded systems are capable of coherent quantum-mechanical motion; but the results are recent and preliminary, and therefore have not yet been fully analyzed. After understanding these results, the next step is to calculate the results for the same set of molecules under different hypothetical orientations, to determine the influence on the System and Bath Heat Currents and understand how these dynamics relate to the nanoscale structural and energetic system parameters.

Conclusion and Future Directions

The methods discussed here have enabled the nanoscale characteristics to be understood in DNA-scaffolded molecular networks, as well as the contributions of their Sites to energy transport. Having multiple approaches like the ones shown here allow diverse systems to be interrogated. Those that are too large for expensive computational work can be probed experimentally and analyzed using machine-learning methods, while the quantum-mechanical heat currents of smaller systems can be understood more precisely using the genetic algorithm and HEOM methods. The coherence lifetimes can also be obtained, providing a substantial suite of tools for understanding how to optimize the coherent motion for quantum-mechanical functions.

The first future direction will be to complete the construction of a 2D electronic spectrometer, which is able to obtain experimental measurements of the coherent dynamics to compare to the computational results. The combination of these techniques will grant both predictive power for strong-performing members, and also experimental corroboration of predictions or simulated results.

The second future direction is to use these methods, which are now developed and working properly, to understand how to control the heat currents based on the molecular parameters. These heat currents are related to dephasing in these systems. As discussed in the introduction, organic systems are usually not considered for quantum information applications because of their fast dephasing, so controlling these characteristics is a high-value target for making these systems more viable for these applications.

Publications and Presentations

The following publications were generated during the Fellowship. An additional one is in progress, but not yet completed.

> Rolczynski, B. S.; Diaz, S. A.; Kim, Y. C.; Mathur, D.; Klein, W. P.; Medintz, I. L.; Melinger, J. S. Determining Interchromophore Effects for Energy Transport in Molecular Networks Using Machine-Learning Algorithms. *Submitted*.
>
> Huff, J.; Diaz, S.; Barclay, M.; Chowdhury, A.; Chiriboga, M.; Ellis, G.; Mathur, D.; Patten, L.; Roy, S.; Sup, A.; Biaggne, A.; Rolczynski, B. S.; Cunningham, P.; Li, L.; Lee, J.; Davis, P.; Yurke, B.; Knowlton, W.; Medintz, I.; Turner, D.; Melinger, J.; Pensack, R. Tunable Electronic Structure via DNA-Templated Heteroaggregates of Two Distinct Cyanine Dyes. J. Phys. Chem. C 2022, 126 (40), 17164-17175.

The following presentations were generated during the Fellowship.

> Rolczynski, B. S.; Diaz, S. A.; Kim, Y. C.; Mathur, D.; Medintz, I. L.; and Melinger, J. S. “Understanding Energy-Transport Bottlenecks In Molecular Networks Using Machine-Learning Tools.” BRICC Conference. Arlington, VA. 9/8/22.
>
> Rolczynski, B. S.; Diaz, S. A.; Kim, Y. C.; Medintz, I. L.; Cunningham, P. D.; and Melinger, J. S. “Understanding Energy Levels and Structures in Modular Chromophore Networks Templated by DNA.” ACS Meeting Fall 2022. Chicago, IL. 8/24/22.
>
> Rolczynski, B. S.; Diaz, S. A.; Kim, Y. C.; Mathur, D.; Medintz, I. L.; and Melinger, J. S. “Machine-Learning Methods for Understanding Energy-Transport in Molecular Networks.” ACS Meeting Fall 2022. Chicago, IL. 8/21/22.
>
> Rolczynski, B. S.; Diaz, S. A.; Kim, Y. C.; Mathur, D.; Medintz, I. L.; Cunningham, P. D.; and Melinger, J. S. “Using Machine-Learning Tools to Understand and Optimize Molecular Networks Templated by DNA.” Mid-Atlantic DNA Nanotechnology Symposium. Rockville, MD. 5/24/22.

References

1. Cardona, T.; Sánchez-Baracaldo, P.; Rutherford, A. W.; Larkum, A. W., Early Archean Origin of Photosystem II. *Geobiology* **2018,** *17* (2), 127-150.

2. Blankenship, R., *Molecular Mechanisms of Photosynthesis*. Wiley: Chichester, 2002.

3. Blankenship, R. E.; Tiede, D. M.; Barber, J.; Brudvig, G. W.; Fleming, G.; Ghirardi, M.; Gunner, M. R.; Junge, W.; Kramer, D. M.; Melis, A.; Moore, T. A.; Moser, C. C.; Nocera, D. G.; Nozik, A. J.; Ort, D. R.; Parson, W. W.; Prince, R. C.; Sayre, R. T., Comparing Photosynthetic and Photovoltaic Efficiencies and Recognizing the Potential for Improvement. *Science* **2011,** *332* (6031), 805-809.

4. Vinyard, D. J.; Ananyev, G. M.; Charles Dismukes, G., Photosystem II: The Reaction Center of Oxygenic Photosynthesis. *Ann. Rev. of Biochem.* **2013,** *82* (1), 577-606.

5. Martínez-Junza, V.; Szczepaniak, M.; Braslavsky, S. E.; Sander, J.; Nowaczyk, M.; Rögner, M.; Holzwarth, A. R., A photoprotection mechanism involving the D2 branch in photosystem II cores with closed reaction centers. *Photochemical & Photobiological Sciences* **2008,** *7* (11), 1337-7.

6. Mukamel, S., *Nonlinear Optical Spectroscopy*. Oxford U. Press: Oxford, 1995.

7. Savikhin, S.; Buck, D. R.; Struve, W. S., Toward Level-to-Level Energy Transfers in Photosynthesis: The Fenna−Matthews−Olson Protein. *J. Phys. Chem. B* **1998,** *102* (29), 5556-5565.

8. Engel, G. S.; Calhoun, T. R.; Read, E. L.; Ahn, T.-K.; Mančal, T. s.; Cheng, Y.-C.; Blankenship, R. E.; Fleming, G. R., Evidence for wavelike energy transfer through quantum coherence in photosynthetic systems. *Nature* **2007,** *446* (7137), 782-786.

9. Wasielewski, M. R.; Forbes, M. D. E.; Frank, N. L.; Kowalski, K.; Scholes, G. D.; Yuen-Zhou, J.; Baldo, M. A.; Freedman, D. E.; Goldsmith, R. H.; Goodson, T.; Kirk, M. L.; McCusker, J. K.; Ogilvie, J. P.; Shultz, D. A.; Stoll, S.; Whaley, K. B., Exploiting chemistry and molecular systems for quantum information science. *Nature Rev. Chem.* **2020**, 1-15.

10. Cao, J.; Cogdell, R. J.; Coker, D. F.; Duan, H.-G.; Hauer, J. r.; Kleinekathöfer, U.; Jansen, T. L. C.; Mančal, T. s.; Miller, R. J. D.; Ogilvie, J. P.; Prokhorenko, V. I.; Renger, T.; Tan, H.-S.; Tempelaar, R.; Thorwart, M.; Thyrhaug, E.; Westenhoff, S.; Zigmantas, D., Quantum biology revisited. *Sci. Adv.* **2020,** *6*, 1-12.

11. Dowling, J. P.; Milburn, G. J., Quantum technology: the second quantum revolution. *Phil. Trans. R. Soc. Lond. A* **2003,** *361* (1809), 1655-1674.

12. Rebentrost, P.; Mohseni, M.; Aspuru-Guzik, A., Role of Quantum Coherence and Environmental Fluctuations in Chromophoric Energy Transport. *J. Phys. Chem. B* **2009,** *113* (29), 9942-9947.

13. O’Brien, J. L., Optical Quantum Computing. *Science* **2007,** *318*, 1567-1570.

14. Cirac, J. I.; Zoller, P., Quantum Computations with Cold Trapped Ions. *Phys. Rev. Lett.* **2011,** *74*, 4091-4094.

15. Gaita-Ariño, A.; Luis, F.; Hill, S.; Coronado, E., Molecular spins for quantum computation. *Nature Chem.* **2019**, 1-9.

16. Acosta, V.; Hemmer, P., Nitrogen-vacancy centers: Physics and applications. *MRS Bullet.* **2013,** *38*, 127-130.

17. Wendin, G., Quantum information processing with superconducting circuits: a review. *Rep. Prog. Phys.* **2017,** *80* (10), 106001-51.

18. Castellanos, M. A.; Dodin, A.; Willard, A. P., On the design of molecular excitonic circuits for quantum computing: the universal quantum gates. *Phys. Chem. Chem. Phys.* **2020,** *22*, 3048-3057.
19. Fratini, S.; Mayou, D.; Ciuchi, S., The Transient Localization Scenario for Charge Transport in Crystalline Organic Materials. *Adv. Func. Mater.* **2016,** *26* (14), 2292-2315.
20. Rolczynski, B. S.; Díaz, S. A.; Kim, Y. C.; Medintz, I. L.; Cunningham, P. D.; Melinger, J. S., Understanding Disorder, Vibronic Structure, and Delocalization in Electronically Coupled Dimers on DNA Duplexes. *J. Phys. Chem. A* **2021,** *125*, 9632-9644.
21. Kalra, S.; Rahnamayan, S.; Deb, K., Enhancing clearing-based niching method using Delaunay Triangulation. *IEEE CEC* **2017**, 2328-2337.
22. Markovitsi, D.; Germain, A.; Millie, P.; Lecuyer, P.; Gallos, L. K.; Argyrakis, P.; Bengs, H.; Ringsdorf, H., Triphenylene Columnar Liquid Crystals: Excited States and Energy Transfer. *J. Phys. Chem* **1995,** *99*, 1005-1017.
23. Tanimura, Y.; Kubo, R., Time Evolution of a Quantum System in Contact with a Nearly Gaussian-Markoffian Noise Bath. *J. Phys. Soc. of Japan* **1989,** *58*, 101-114.
24. Tanimura, Y., Numerically “exact” approach to open quantum dynamics: The hierarchical equations of motion (HEOM). *J. Chem. Phys.* **2020,** *153*, 020901.
25. Tanimura, Y., Stochastic Liouville, Langevin, Fokker–Planck, and Master Equation Approaches to Quantum Dissipative Systems *J. Phys. Soc. of Japan* **2006,** *75*, 082001.
26. Maillard, J.; Klehs, K.; Rumble, C.; Vauthey, E.; Heilemann, M.; Fürstenberg, A., Universal quenching of common fluorescent probes by water and alcohols. *Chem. Sci.* **2021**, 1352-1362.
27. Sobakinskaya, E.; Busch, M. S. a.; Renger, T., Theory of FRET “Spectroscopic Ruler” for Short Distances: Application to Polyproline. *J. Phys. Chem. B* **2017,** *122*, 54-67.
28. Ishizaki, A.; Fleming, G. R., Unified treatment of quantum coherent and incoherent hopping dynamics in electronic energy transfer: Reduced hierarchy equation approach. *J. Chem. Phys.* **2009,** *130* (23), 234111.
29. Ma, J.; Cao, J., Förster resonance energy transfer, absorption and emission spectra in multichromophoric systems. I. Full cumulant expansions and system-bath entanglement. *J. Chem. Phys.* **2015,** *142* (9), 094106.
30. Yeh, S.-H.; Kais, S., Simulated two-dimensional electronic spectroscopy of the eight-bacteriochlorophyll FMO complex. *J. Chem. Phys.* **2014,** *141* (23), 234105.
31. Liu, H.; Zhu, L.; Bai, S.; Shi, Q., Reduced quantum dynamics with arbitrary bath spectral densities: Hierarchical equations of motion based on several different bath decomposition schemes. *J. Chem. Phys.* **2014,** *140* (13), 134106.
32. Ishizaki, A.; Tanimura, Y., Quantum Dynamics of System Strongly Coupled to Low-Temperature Colored Noise Bath: Reduced Hierarchy Equations Approach. *J. Phys. Soc. of Japan* **2005,** *74* (12), 3131-3134.
33. Strümpfer, J.; Schulten, K., Open Quantum Dynamics Calculations with the Hierarchy Equations of Motion on Parallel Computers. *J. Chem. Theory and Comput.* **2012,** *8*, 2808-2816.
34. Johansson, J. R.; Nation, P. D.; Nori, F., QuTiP 2: A Python framework for the dynamics of open quantum systems. *Comput. Phys. Commun.* **2013,** *184* (4), 1234-1240.
35. Johansson, J. R.; Nation, P. D.; Nori, F., QuTiP: An open-source Python framework for the dynamics of open quantum systems. *Comput. Phys. Commun.* **2012,** *183* (8), 1760-1772.

36. Kato, A.; Tanimura, Y., Quantum heat current under non-perturbative and non-Markovian conditions: Applications to heat machines. *The Journal of Chemical Physics* **2016,** *145*, 224105.

37. Kato, A.; Tanimura, Y., Quantum heat transport of a two-qubit system: Interplay between system-bath coherence and qubit-qubit coherence. *The Journal of Chemical Physics* **2015,** *143*, 064107.

38. Breiman, L., Random Forests. *Machine Learning* **2001,** *45*, 5-32.

39. Hastie, T.; Tibshirani, R.; Friedman, J., *The Elements of Statistical Learning*. Second ed.; Springer: New York, 2009.

40. Rolczynski, B. S.; Diaz, S. A.; Kim, Y. C.; Mathur, D.; Klein, W. P.; Medintz, I. L.; Melinger, J. S., Determining Interchromophore Effects for Energy Transport in Molecular Networks Using Machine-Learning Algorithms.

41. Ishizaki, A.; Fleming, G. R., On the adequacy of the Redfield equation and related approaches to the study of quantum dynamics in electronic energy transfer. *J. Chem. Phys.* **2009,** *130* (23), 234110.

42. Klein, W. P.; Díaz, S. A.; Buckhout-White, S.; Melinger, J. S.; Cunningham, P. D.; Goldman, E. R.; Ancona, M. G.; Kuang, W.; Medintz, I. L., Utilizing HomoFRET to Extend DNA-Scaffolded Photonic Networks and Increase Light-Harvesting Capability. *Adv. Opt. Mater.* **2016,** *6* (1), 1700679-12.